Monthly Notices
of the
ROYAL ASTRONOMICAL SOCIETY

MNRAS 475, 3959–3973 (2018) doi:10.1093/mnras/sty066
Advance Access publication 2018 January 10

SN 2016X: a type II-P supernova with a signature of shock breakout from explosion of a massive red supergiant

F. Huang,[1,2,3★] X.-F. Wang,[1] G. Hosseinzadeh,[4,5] P. J. Brown,[6] J. Mo,[1] J.-J. Zhang,[3,7,8] K.-C. Zhang,[1] T.-M. Zhang,[9] D.-A. Howell,[4,5] I. Arcavi,[4,5†] C. McCully,[4,5] S. Valenti,[10] L.-M. Rui,[1] H. Song,[1] D.-F. Xiang,[1] W.-X. Li,[1] H. Lin[1] and L.-F. Wang[6]

[1]*Physics Department and Tsinghua Centre for Astrophysics, Tsinghua University, Beijing 100084, China*
[2]*Department of Astronomy, Shanghai Jiao Tong University, Shanghai 200240, China*
[3]*Key Laboratory for the Structure and Evolution of Celestial Objects, Chinese Academy of Sciences, Kunming 650011, China*
[4]*Department of Physics, University of California, Santa Barbara, CA 93106-9530, USA*
[5]*Las Cumbres Observatory, 6740 Cortona Dr, Suite 102, Goleta, CA 93117-5575, USA*
[6]*Department of Physics and Astronomy, George P. and Cynthia Woods Mitchell Institute for Fundamental Physics and Astronomy, Texas A&M University, 4242 TAMU, College Station, TX 77843, USA*
[7]*Yunnan Observatories, Chinese Academy of Sciences, Kunming 650011, China*
[8]*Centre for Astronomical Mega-Science, Chinese Academy of Sciences, 20A Datun Road, Chaoyang District, Beijing 100012, China*
[9]*Key Laboratory of Optical Astronomy, National Astronomical Observatories, Chinese Academy of Sciences, Beijing 100012, China*
[10]*Department of Physics, University of California, 1 Shields Avenue, Davis, CA 95616-5270, USA*

Accepted 2018 January 3. Received 2017 December 18; in original form 2017 November 8

ABSTRACT

We present extensive ultraviolet (UV) and optical photometry, as well as dense optical spectroscopy, for type II Plateau (IIP) supernova SN 2016X that exploded in the nearby (∼15 Mpc) spiral galaxy UGC 08041. The observations span the period from 2 to 180 d after the explosion; in particular, the *Swift* UV data probably captured the signature of shock breakout associated with the explosion of SN 2016X. It shows very strong UV emission during the first week after explosion, with a contribution of ∼20–30 per cent to the bolometric luminosity (versus $\lesssim$15 per cent for normal SNe IIP). Moreover, we found that this supernova has an unusually long rise time of about 12.6 ± 0.5 d in the *R* band (versus ∼7.0 d for typical SNe IIP). The optical light curves and spectral evolution are quite similar to the fast-declining type IIP object SN 2013ej, except that SN 2016X has a relatively brighter tail. Based on the evolution of photospheric temperature as inferred from the *Swift* data in the early phase, we derive that the progenitor of SN 2016X has a radius of about 930 ± 70 $R_\odot$. This large-size star is expected to be a red supergiant star with an initial mass of $\gtrsim$19–20 $M_\odot$ based on the mass–radius relation of the Galactic red supergiants, and it represents one of the most largest and massive progenitors found for SNe IIP.

Key words: supernovae: general – supernovae: individual: SN 2016X – galaxies: individual: UGC 08041.

1 INTRODUCTION

Type II supernovae (SNe) are the outcome of massive stars (with initial mass ≥8 $M_\odot$; e.g. Nomoto 1984; Nomoto & Hashimoto 1988; Smartt 2009; Ibeling & Heger 2013) experiencing gravitational core collapse after energy exhaustion at the end of life. They are characterized by P-cygni profile of Balmer lines in the early optical spectra compared to type I SNe (Filippenko 1997). Based on the behaviours of light curves, SNe II are further divided into two subclasses: those with a prolonged plateau lasting ∼100 d are called type IIP, while those with a linear decline trend after maximum belong to type IIL (Barbon, Ciatti & Rosino 1979). Recently, statistical work with large samples from different surveys tends to favour for a continuum distribution of the observational properties of SNe II (e.g. Anderson et al. 2014; Sanders et al. 2015; Valenti et al. 2016). As the most abundant subtype, SNe IIP occupy about 70 per cent of all observed SNe II in a volume-limited sample (Li et al. 2011). The observed plateau in the light curve results from the propagation of a cooling and recombination wave through the

★ E-mail: huangfang@sjtu.edu.cn
† Einstein Fellow.

SN envelope (Grassberg et al. 1971; Grasberg & Nadezhin 1976). The presence of prominent hydrogen lines indicates that they retain a significant fraction of hydrogen envelopes before explosion.

Analysis of the archive images allows direct detections of the progenitors for a few SNe IIP, which are generally found to be red supergiant (RSG) stars with a mass range of 8.5–16.5 $M_{\odot}$ (Smartt 2009, 2015). The observational limit is lower than the prediction from theoretical models, e.g. 8–25 $M_{\odot}$ (Ekström et al. 2012). This inconsistency might be somewhat related to the presence of substantial circumstellar dust around the RSGs, which could lead to the underestimate of luminosity and hence the initial mass of the progenitor stars (Fraser et al. 2012; Van Dyk et al. 2012; Dall'Ora et al. 2014). SNe IIP show a large diversity in the observational properties, such as peak luminosity, plateau length, expansion velocity, and synthesized nickel mass (Hamuy 2003). These are connected with the explosion mechanism and the physical characteristics of the progenitors such as mass, explosion energy, and initial radius (Kasen & Woosley 2009; Pumo & Zampieri 2011). Dozens of SNe IIP have been extensively studied from the ultraviolet (UV) to the near-infrared wavelength, i.e. SN 2005cs (Pastorello et al. 2009), SN 2009N (Takáts et al. 2014), and SN 2013ej (Valenti et al. 2014; Huang et al. 2015), which helps take a deep look into the observed diversity and the progenitor physics. SN 2016X provides another opportunity for such kind of study.

SN 2016X (ASASSN-16at) was discovered by All Sky Automated Survey for SuperNovae (ASAS-SN) on 2016 January 20.59 (UT dates are used throughout this paper) in the nearby SBd galaxy UGC 08041 ($z = 0.004\,408$ from NED) at a V-band magnitude of ∼15.1 mag. The J2000 coordinates of the SN are $\alpha = 12^{\mathrm{h}}55^{\mathrm{m}}15\overset{\mathrm{s}}{.}50$ and $\delta = +00°05'59\overset{''}{.}7$, approximately 60 arcsec south and 42 arcsec east from the centre of UGC 08041 (Bock et al. 2016). The last non-detection was reported on January 18.35 with a limit of $V > 18.0$ mag, but it was detected on 2016 January 19.49 at $V \sim 16.6$ mag and January 19.50 at $V \sim 17.0$ mag. We therefore adopt 2016 January 18.9 (MJD = 57405.92 ± 0.57) as the explosion time. An optical spectrum obtained on January 20.75 suggests that it is a young core-collapse SN (Hosseinzadeh et al. 2016), while another spectrum obtained on January 23.88 confirms that it is a type II-P SN (Zheng & Zhang 2016). Grupe et al. (2016) reported the discovery of X-rays from SN 2016X with *Swift*, which indicates that SN 2016X may have experienced moderate interaction with circumstellar material or stellar wind at early phase. We therefore triggered an instant follow-up campaign to study the photometric and spectroscopic evolution of this young type II-P SN. The distance to its host galaxy is estimated to be 15.2 Mpc (distance modulus $\mu = 30.91 \pm 0.43$ mag) using Tully–Fisher method (Sorce et al. 2014), which is adopted throughout this work.

In this paper, we present photometry and spectroscopy of the nearby type IIP SN 2016X. In Section 2, we describe the observations and data reduction process for photometric and spectroscopic data. In Section 3, we study the photometric behaviour of SN 2016X. The spectroscopic evolution is presented in Section 2.2. We discuss the explosion parameters and progenitor properties of SN 2016X in Section 5, and summarize our conclusions in Section 6.

2 OBSERVATIONS AND DATA REDUCTION

2.1 Photometry

2.1.1 *Ground-based observation*

High-cadence, broad-band photometric data of SN 2016X were obtained in Johnson *UBV* and Sloan *gri* filters with the 1.0-m telescopes of Las Cumbres Observatory (LCO; Brown et al. 2013), spanning from 2016 January 21 to July 6. We also used the 0.8-m Tsinghua University-NAOC telescope (TNT; Wang et al. 2008; Huang et al. 2012) at Xinglong Observatory and the Lijiang 2.4-m telescope (LJT; Fan et al. 2015) of Yunnan Astronomical Observatories in China to collect photometry in Johnson–Cousin *UBVRI* filters. The observations began on 2016 January 23 and ended on 2016 June 3.

All data were pre-processed with standard IRAF[1] routines, including the corrections for bias, overscan, flat-field, and cosmic ray removal. For TNT and LJT data, instrumental magnitudes were determined using the point spread function (PSF) photometry with the SNOOPY package.[2] The LCO data were reduced using `lcogtsnpipe` (Valenti et al. 2016). The colour terms and extinction coefficients were derived from observations of Landolt stars on photometric nights (Landolt 1992). The photometric zero-points were determined by comparing the magnitudes of 10 field stars (marked in Fig. 1) to the values transformed from the Sloan Digital Sky Survey (SDSS) Data Release 9 catalogue (Ahn et al. 2012) using the relation from Chonis & Gaskell (2008). The coordinates and magnitudes of the reference stars around SN 2016X are listed in Table 1, and the final calibrated magnitudes of SN 2016X are presented in Tables 2–4.

2.1.2 *Swift UVOT observations*

SN 2016X was also observed in the UV and optical bands with the Ultra-Violet/Optical Telescope (UVOT; Roming et al. 2005) on board the *Swift* spacecraft (Gehrels et al. 2004). The space-based observations were obtained in the *uvw*2, *uvm*2, *uvw*1, *u*, *b*, and *v* filters, covering the period from 2016 January 21 to March 5, and these data were taken from the *Swift* Optical/Ultraviolet Supernova Archive[3] (SOUSA; Brown et al. 2014). The data reduction is based on the method described in Brown et al. (2009), including subtraction of the host galaxy count rates and usage of the revised UV zero-points and time-dependent sensitivity loss from Breeveld et al. (2011). The UVOT magnitudes of SN 2016X are listed in Table 5.

2.2 Spectroscopy

The spectroscopic observations of SN 2016X started on 2016 January 20 and continued until 2016 June 9, corresponding to ∼2 d to ∼140 d after the explosion. A total of 40 low-resolution optical spectra were collected using the LCO 2-m Faulkes Telescope North (FTN; with FLOYDS), the Lijiang 2.4-m telescope (with YFOSC; Fan et al. 2016), and the Xinglong 2.16-m telescope (with BFOSC). A journal of spectroscopic observations is given in Table 6.

The spectroscopic data were reduced in a standard manner under the IRAF environment. After bias and overscan corrections, and flat-fielding and cosmic ray removal, one-dimensional spectra were extracted using the optimal extraction method (Horne 1986). The wavelength calibration was done using the Fe/Ar and Hg/Ar lamp spectra, and the fluxes were calibrated using spectrophotometric standards observed on the same night with the same instrumental

[1] IRAF is distributed by the National Optical Astronomy Observatories, which are operated by the Association of Universities for Research in Astronomy, Inc., under cooperative agreement with the National Science Foundation (NSF).

[2] http://sngroup.oapd.inaf.it/snoopy.html

[3] http://swift.gsfc.nasa.gov/docs/swift/sne/swift_sn.html

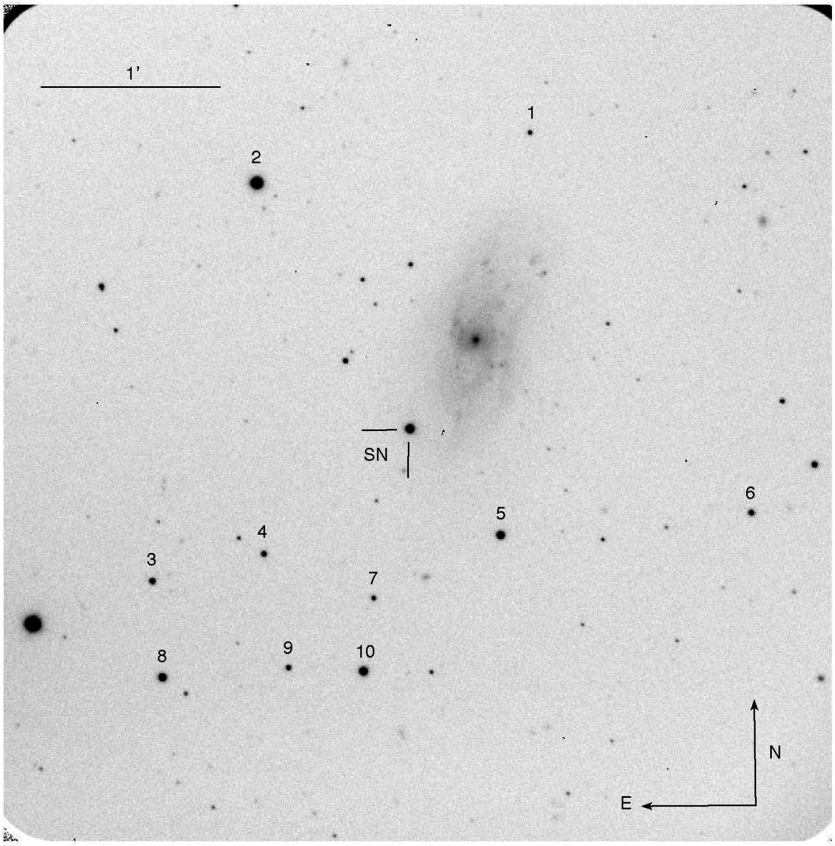

Figure 1. SN 2016X in UGC 08041. The *R*-band image of the field of SN 2016X was taken on 2016 March 3 with the Lijiang 2.4-m telescope. SN 2016X and the 10 reference stars are marked.

Table 1. Photometric standard stars in the field of SN 2016X (1σ uncertainties).

Star ID	α_{J2000} (h m s)	δ_{J2000} (° ′ ″)	U (mag)	B (mag)	V (mag)	R (mag)	I (mag)
1	12:55:10.458	0:09:19.79	18.58(03)	18.38(04)	17.58(03)	17.11(03)	16.66(06)
2	12:55:22.596	0:08:42.00	14.47(02)	13.91(03)	13.47(02)	13.10(05)	12.39(09)
3	12:55:26.850	0:04:14.02	18.81(04)	17.78(06)	16.62(03)	15.95(04)	15.33(09)
4	12:55:21.901	0:04:33.88	17.92(03)	17.59(05)	16.77(03)	16.29(04)	15.81(07)
5	12:55:11.357	0:04:50.16	18.38(03)	17.24(07)	15.72(04)	14.78(08)	13.72(16)
6	12:55:00.181	0:05:08.91	16.93(02)	17.05(04)	16.48(03)	16.14(03)	15.78(05)
7	12:55:16.953	0:04:05.97	20.37(08)	19.44(07)	17.94(04)	16.92(10)	15.56(21)
8	12:55:26.305	0:03:09.69	16.20(02)	15.98(04)	15.30(03)	14.90(03)	14.49(06)
9	12:55:14.299	0:03:17.25	19.16(04)	18.97(04)	18.27(03)	17.85(03)	17.41(06)
10	12:55:17.333	0:03:16.92	15.72(02)	15.68(04)	15.01(03)	14.60(03)	14.15(06)

set-up. FLOYDS spectra were reduced using the `floydsspec` pipeline.

3 PHOTOMETRIC EVOLUTION

The light curves of SN 2016X in UV and optical bands are shown in Fig. 2, ranging from 2 to 170 d after explosion. The UV luminosity rises to the peak in a short time, followed by a rapid decline. The optical light curves resemble the evolution of typical SNe IIP but with relatively faster declines during the plateau phase. We present detailed analysis in the following subsections.

3.1 *Swift* UV light curves

The *Swift* UVOT observations of SN 2016X were triggered immediately after its discovery. The very early light curves in the *uvw*2 and *uvm*2 bands show an initial decline before rising to the peak at t ~5 d after explosion (see the insert panel of Fig. 2). This indicates that SN 2016X may have another UV peak within 1–2 d from the explosion, which could be due to the breakout of a blast shockwave through the progenitor star's outer envelope after the core-collapse explosion (Falk & Arnett 1977; Klein & Chevalier 1978). The observed UV trough might thus be associated with the cooling of shock breakout, when the temperature behind the shock is lower than that at the shock front (Schawinski et al. 2008). Such

Table 2. Optical photometry from TNT.

UT date (yy/mm/dd)	MJD	Phase[a] (d)	U (mag)	B (mag)	V (mag)	R (mag)	I (mag)
2016 Jan. 30	57417.705	11.79	13.28(01)	14.26(03)	14.11(01)	13.95(01)	13.78(04)
2016 Jan. 31	57418.755	12.84	13.19(01)	14.32(02)	14.09(02)	13.89(03)	13.77(02)
2016 Feb. 01	57419.885	13.97	13.46(01)	14.28(04)	14.10(04)	13.89(05)	13.75(05)
2016 Feb. 02	57420.710	14.79	13.61(02)	14.44(03)	14.16(04)	14.06(05)	93.94(04)
2016 Feb. 04	57422.775	16.86	–	14.44(03)	14.21(03)	13.99(03)	13.82(02)
2016 Feb. 05	57423.870	17.95	13.88(02)	14.51(03)	14.26(04)	14.00(02)	13.84(04)
2016 Feb. 14	57432.680	26.76	14.82(01)	14.96(02)	14.41(01)	14.13(03)	13.91(02)
2016 Feb. 15	57433.885	27.97	14.97(02)	15.01(03)	14.46(01)	14.15(04)	13.99(02)
2016 Feb. 16	57434.690	28.77	15.03(02)	15.07(02)	14.49(03)	14.16(03)	13.99(04)
2016 Feb. 17	57435.695	29.78	15.24(02)	15.09(03)	14.49(04)	14.13(05)	13.99(04)
2016 Feb. 19	57437.885	31.97	–	15.19(03)	14.53(03)	14.21(02)	13.98(03)
2016 Feb. 20	57438.675	32.76	15.40(03)	15.20(04)	14.60(04)	14.21(04)	14.04(04)
2016 Feb. 22	57440.705	34.79	–	15.24(01)	14.58(02)	14.20(01)	14.03(01)
2016 Feb. 23	57441.885	35.97	–	15.33(03)	14.54(03)	14.28(04)	–
2016 Mar. 01	57448.845	42.93	15.93(04)	15.65(03)	14.74(04)	14.36(06)	14.14(05)
2016 Mar. 02	57449.690	43.77	15.96(05)	15.51(03)	14.72(04)	14.29(04)	14.07(05)
2016 Mar. 03	57450.670	44.75	–	15.52(02)	14.67(03)	14.28(03)	14.09(03)
2016 Mar. 05	57452.625	46.71	15.98(05)	15.56(05)	14.67(05)	14.22(04)	14.03(05)
2016 Mar. 10	57457.635	51.72	16.12(03)	15.61(05)	14.66(05)	14.26(05)	14.03(04)
2016 Mar. 11	57458.645	52.73	16.12(05)	15.60(04)	14.75(02)	14.31(03)	14.08(03)
2016 Mar. 12	57459.630	53.71	16.26(04)	15.70(04)	14.87(04)	14.40(04)	14.18(04)
2016 Mar. 13	57460.625	54.71	16.23(05)	15.70(04)	14.66(07)	14.30(06)	14.05(04)
2016 Mar. 20	57467.715	61.80	16.43(07)	15.85(03)	14.81(04)	14.46(05)	14.17(05)
2016 Mar. 29	57476.685	70.77	17.02(05)	16.13(03)	15.00(04)	14.54(03)	14.30(04)
2016 Mar. 30	57477.695	71.78	17.18(07)	16.11(04)	15.04(03)	14.60(06)	14.32(04)
2016 Apr. 03	57481.750	75.83	17.35(05)	16.24(02)	15.04(01)	14.61(04)	14.28(03)
2016 Apr. 04	57482.750	76.83	17.39(09)	16.22(03)	15.11(03)	14.59(03)	14.33(05)
2016 Apr. 13	57491.750	85.83	17.80(07)	16.55(03)	15.23(03)	14.71(03)	14.48(03)
2016 Apr. 16	57494.750	88.83	18.40(14)	16.75(03)	15.42(04)	14.84(04)	14.58(02)
2016 Apr. 22	57500.750	94.83	–	–	15.87(05)	15.25(05)	14.91(03)
2016 Apr. 23	57501.750	95.83	–	17.41(10)	16.18(04)	15.44(03)	15.03(03)
2016 May 06	57514.500	108.58	19.59(34)	18.14(05)	16.77(03)	16.05(04)	15.67(04)
2016 May 07	57515.750	109.83	–	–	–	16.14(17)	15.76(17)
2016 Jun. 02	57541.500	135.58	–	18.36(05)	17.23(04)	16.53(03)	16.20(03)

[a]Relative to the explosion date, MJD = 57405.92.

a UV trough had ever been reported for two SNe IIP at relatively larger distances, i.e. SNLS-04D2dc (Schawinski et al. 2008) and SNLS-06D1jd (Gezari et al. 2008).

By adopting a polynomial fitting to the early data, we obtained $m_{uvw2}(\max) = 12.79$ mag on 4.53 d, $m_{uvm2}(\max) = 12.61$ mag on 4.88 d, and $m_{uvw1}(\max) = 12.68$ mag on 5.02 d relative to the explosion date. The rise time for the primary UV peaks is ∼2 d longer than that of SNLS-04D2dc and SNLS-06D1jd, indicating that SN 2016X may have a progenitor with a larger initial radius. After the maximum, the SN declines quickly in the *swift uvw*2, *uvm*2, *uvw*1, and *u* bands, with a rate of 0.245 ± 0.012, 0.269 ± 0.022, 0.208 ± 0.027, and 0.135 ± 0.011 mag d^{-1}, respectively. While the corresponding decay rate is 0.047 ± 0.011, and 0.016 ± 0.014 mag d^{-1} in *swift b* and *v* bands. Note that SN 2016X shows a faster decline in *uvm*2 than in *uvw*2 and *uvw*1, which is against the usual trend that the decay rate steepens at shorter wavelengths. This opposite trend is also seen in other SNe IIP (i.e. SN 2005cs), and it might be related to the fact that more Fe III and Fe II lines are concentrated within the *uvm*2 bandpass (Brown et al. 2007).

Fig. 3 shows *Swift* UVOT absolute light curves of SN 2016X and some well-observed SNe IIP. Extinction corrections have been applied to all of our objects. As it can be seen, SN 2016X lies on the bright side of SNe IIP, and it reached the UV maximum 2–3 d later than other objects with UV observations. After $t \approx 1$ month from the peak, the UV light curves seem to flatten out especially in the *uvw*1 and *uvw*2 filters, and this is similarly seen in SN 2012aw, SN 2013ab, and SN 2013ej. At this phase, the UV emission becomes very weak and the photometry can be significantly affected by optical photons leaked out of the red tails of the UV filters (Brown et al. 2016).

3.2 Optical light curves

The overall evolution of the optical light curves of SN 2016X can be divided into four main phases: the rising phase (∼15 d), the plateau phase (∼90 d), the transitional phase (∼100 d), and the nebular phase (≥ 100 d).

The densely sampled data obtained immediately after the explosion allow us to catch the rising evolution of SN 2016X in very early phase. Using polynomial fit to the observed data around the maximum light, we are able to estimate the dates of maximum light and the peak magnitudes in different filters. The results for the phases of maximum and peak magnitudes in different bands are listed in Table 7.

After the maximum light, the *B*-band magnitude declines by ∼4.0 mag in 100 d, which is larger than the typical value for SNe

Table 3. Optical photometry from Lijiang 2.4-m telescope.

UT date (yy/mm/dd)	MJD	Phase[a] (d)	U (mag)	B (mag)	V (mag)	R (mag)	I (mag)
2016 Jan. 23	57410.91	4.99	13.36(02)	14.29(04)	14.38(03)	14.31(04)	14.33(02)
2016 Jan. 28	57415.92	10.00	13.23(02)	14.02(05)	14.04(04)	14.09(04)	13.81(05)
2016 Feb. 02	57420.88	14.96	13.53(06)	14.38(02)	14.16(02)	13.93(03)	13.83(03)
2016 Feb. 04	57422.83	16.91	13.90(17)	14.49(09)	14.36(08)	14.16(09)	13.95(05)
2016 Feb. 13	57431.92	26.00	14.88(05)	14.86(05)	14.37(02)	14.10(01)	13.90(08)
2016 Feb. 16	57434.85	28.93	15.19(02)	15.06(02)	14.48(02)	14.17(02)	14.02(01)
2016 Feb. 18	57436.90	30.98	15.27(03)	15.27(03)	14.69(03)	14.23(03)	14.06(01)
2016 Feb. 23	57441.84	35.92	15.79(03)	15.45(02)	14.67(05)	14.30(07)	14.06(11)
2016 Feb. 28	57446.83	40.91	15.83(07)	15.49(08)	14.62(05)	14.41(09)	–
2016 Mar. 02	57449.93	44.01	15.96(02)	15.47(03)	14.72(02)	14.32(03)	14.08(02)
2016 Mar. 03	57450.84	44.92	15.96(04)	15.49(02)	14.69(03)	14.26(03)	14.07(03)
2016 Mar. 11	57458.85	52.93	16.21(03)	15.59(04)	14.75(02)	14.30(06)	14.09(02)
2016 Mar. 16	57460.91	54.99	16.36(13)	15.78(06)	14.86(04)	14.45(03)	14.14(03)
2016 Mar. 18	57465.74	59.82	16.66(12)	15.89(04)	14.85(04)	–	–
2016 Mar. 20	57467.88	61.96	–	15.86(01)	14.92(02)	14.46(02)	14.21(02)
2016 Apr. 04	57482.75	76.83	–	16.39(03)	15.09(04)	14.63(04)	14.37(02)
2016 Apr. 09	57487.73	81.81	17.56(08)	16.39(04)	15.19(03)	14.68(04)	14.41(01)
2016 Apr. 17	57495.79	89.87	–	17.05(15)	15.45(12)	14.96(03)	14.51(05)
2016 Apr. 26	57504.72	98.80	19.36(16)	18.00(06)	16.58(04)	15.83(04)	15.51(06)
2016 May 02	57510.68	104.76	–	–	16.92(03)	16.23(05)	15.85(04)
2016 May 11	57519.69	113.77	19.66(33)	18.03(13)	16.88(06)	16.26(07)	15.96(06)
2016 May 27	57535.70	129.78	–	18.30(06)	17.08(03)	16.40(03)	16.07(02)
2016 Jun. 03	57542.67	136.75	–	18.29(14)	17.17(09)	16.55(05)	16.17(05)

[a]Relative to the explosion date, MJD = 57405.92.

IIP (i.e. $\beta^{B}_{100} < 3.5$ mag; Patat et al. 1994). The V band declines by $\sim$0.8 mag from the peak brightness in the first 50 d after explosion, which is also larger than normal SNe IIP (i.e. $s50_V < 0.5$ mag; Faran et al. 2014). Moreover, there are a few luminous SNe IIP (e.g. SNe 2007od, 2007pk, 2009bw, 2009dd, and 2013ej) that are found to show similar large post-maximum magnitude declines (Inserra et al. 2011, 2012, 2013; Huang et al. 2015; Valenti et al. 2015). This indicates that a larger V band decline should be used to make a distinguish between SNe IIP and SNe IIL, or these fast-declining SNe IIP may actually represent a subclass linking normal SNe IIP and SNe IIL. From the end of the plateau phase, the SN starts a transitional phase with a very rapid flux drop. For example, the V-band magnitude drops by $\sim$2.0 mag during the phase from $t \approx +90$ d to $+130$ d. After $t \approx 110$ d, the SN enters into the nebular phase powered by the radioactive decay (i.e. ^{56}Co to ^{56}Fe). The decline rates at this phase are estimated to be 0.79, 1.44, 1.22, and 1.14 mag $(100\,\mathrm{d})^{-1}$ in $BVRI$ bands, respectively.

3.3 Rise time

The rise time is an important parameter to constrain the properties of progenitor and explosion physics of SNe, which is typically defined as the time between the explosion epoch and the maximum light. Following the definition by Gall et al. (2015), we adopt the maximum-light date as the time when the r/R-band magnitude rises by less than 0.01 mag d^{-1}.

Based on a sample of 20 SNe IIP and IIL, Gall et al. (2015) found that SNe II show a diversity of rise time, with an average value of 7.0 ± 0.3 d for SNe IIP. The rise time is found to depend more sensitively on the progenitor radius than the mass and explosion energy (Rabinak & Waxman 2011). On the other side, recent studies indicate that the rise time of SNe II only shows a weak correlation with their luminosities (Rubin et al. 2016; Valenti et al. 2016). This is in contrast to previous conclusion that brighter SNe II tend to have longer rise time (Gal-Yam et al. 2011; Valenti et al. 2014; Gall et al. 2015).

Fitting a low-order polynomial to the data around maximum, we find that the r-band light curve has a rise time of 12.6 ± 0.5 d for SN 2016X, and an absolute peak magnitude of -17.00 ± 0.43 mag. Fig. 4 shows the comparison of r/R-band light curves and rise time between SN 2016X and some SNe II with early photometry. One can see that SN 2016X has a longer rise time than typical SNe IIP, while the absolute magnitude at the end of rise follows the brighter slower trend. The longer rise time of SN 2016X indicates that its initial radius should be larger than that of normal SNe IIP, as predicted by the fact that photons take longer time to reach the surface of exploding star.

3.4 Reddening and colour curves

The Galactic reddening along the line of sight to SN 2016X is $E(B-V)_{\mathrm{MW}} = 0.02$ mag (Schlafly & Finkbeiner 2011). The host galaxy reddening is estimated using the colour method raised by Olivares et al. (2010) which assumes that the intrinsic $V-I$ colour is constant [i.e. $(V-I)_0 = 0.656$ mag] towards the end of the plateau phase. Fitting the V-band light curve with equation 4 from Olivares et al. (2010), we obtain the middle of the transition phase as $t_{\mathrm{PT}} = 95$ d. Using the $V-I$ colour at 65 d and correcting for the Galactic reddening, we obtain $A_v(\mathrm{host}) = 0.05 \pm 0.21$ mag. Thus, we adopt the extinction $E(B-V)_{\mathrm{tot}} = 0.04$ mag for SN 2016X.

In Fig. 5, we show the reddening corrected $(U-B)_0$, $(B-V)_0$, $(V-R)_0$, and $(V-I)_0$ colour curves of SN 2016X together with those of a few comparison SNe IIP. The colour evolution of SN 2016X shows similar trend with that of other SNe IIP. At early time, the $(U-B)_0$ and $(B-V)_0$ colours are quite blue and they evolve towards redder colours rapidly as a result of faster expansion and cooling of the ejecta. In comparison, the $(V-R)_0$ and $(V-I)_0$ colours evolve more slowly with a rate of < 0.5 mag in 30 d. During

Table 4. Optical photometry from LCO (1σ uncertainties).

UT date (yy/mm/dd)	MJD	Phase[a] (d)	U (mag)	B (mag)	V (mag)	g (mag)	r (mag)	i (mag)
2016 Jan. 21	57408.340	2.421	13.723(023)	14.711(042)	14.818(035)	14.714(032)	14.903(030)	15.021(020)
2016 Jan. 22	57409.360	3.441	13.718(052)	14.504(042)	14.675(041)	14.473(022)	14.775(036)	14.845(042)
2016 Jan. 25	57412.275	6.356	13.615(012)	14.199(044)	14.186(052)	14.265(023)	14.364(047)	14.328(028)
2016 Jan. 26	57413.315	7.396	13.276(023)	14.128(030)	14.083(032)	14.073(033)	14.370(041)	14.258(033)
2016 Jan. 26	57413.340	7.421	13.259(027)	14.130(027)	14.070(026)	14.055(030)	14.147(022)	14.216(026)
2016 Jan. 28	57415.085	9.166	13.300(044)	14.088(038)	14.162(035)	14.026(036)	14.159(040)	14.274(039)
2016 Jan. 28	57415.235	9.316	13.276(041)	14.162(032)	14.198(034)	14.113(041)	14.095(050)	14.106(048)
2016 Feb. 01	57419.245	13.326	13.509(052)	14.288(041)	14.109(029)	14.150(026)	14.043(024)	14.176(028)
2016 Feb. 03	57421.090	15.171	13.565(016)	14.348(041)	13.991(026)	14.168(044)	14.023(032)	14.161(032)
2016 Feb. 07	57425.095	19.176	14.284(018)	14.515(058)	14.261(050)	14.308(029)	14.189(052)	14.211(039)
2016 Feb. 12	57430.655	24.736	14.460(035)	14.790(056)	14.407(054)	14.513(030)	14.222(038)	14.315(035)
2016 Feb. 15	57433.995	28.076	14.995(073)	15.067(042)	–	14.631(043)	14.269(040)	14.387(043)
2016 Feb. 19	57437.720	31.801	–	15.178(053)	14.490(038)	14.870(036)	14.342(034)	14.381(025)
2016 Feb. 23	57441.565	35.646	15.356(037)	15.323(044)	14.682(039)	14.888(045)	14.486(042)	14.467(029)
2016 Feb. 28	57446.035	40.116	15.689(032)	15.426(032)	14.657(039)	14.973(037)	14.533(039)	14.500(038)
2016 Mar. 02	57449.765	43.846	–	–	–	14.985(036)	14.548(053)	14.516(025)
2016 Mar. 08	57455.340	49.421	–	15.628(062)	14.710(042)	15.285(042)	14.454(035)	14.502(034)
2016 Mar. 11	57458.665	52.746	15.881(057)	15.621(045)	14.787(029)	15.314(052)	14.613(037)	14.487(033)
2016 Mar. 16	57463.075	57.156	16.141(063)	15.769(052)	14.799(017)	–	–	–
2016 Mar. 18	57465.255	59.336	16.195(049)	15.864(031)	14.843(039)	15.345(028)	14.572(030)	14.532(022)
2016 Mar. 21	57468.915	62.996	16.425(100)	15.967(048)	14.914(031)	15.330(043)	14.609(031)	14.629(035)
2016 Mar. 30	57477.110	71.191	–	16.178(046)	15.027(039)	15.503(031)	14.728(035)	14.757(038)
2016 Apr. 02	57480.830	74.911	16.855(065)	16.252(044)	15.045(034)	15.574(036)	14.824(040)	14.783(028)
2016 Apr. 07	57485.535	79.616	17.352(171)	16.305(050)	15.126(038)	15.588(031)	14.780(028)	14.799(032)
2016 Apr. 10	57488.785	82.866	17.925(144)	16.512(047)	15.213(047)	15.719(030)	14.891(044)	14.876(044)
2016 Apr. 15	57493.775	87.856	97.478(250)	16.829(062)	15.361(039)	15.939(032)	15.012(027)	15.000(032)
2016 Apr. 22	57500.465	94.546	–	17.227(058)	15.943(037)	16.401(034)	15.444(041)	15.363(040)
2016 Apr. 26	57504.740	98.821	–	17.973(062)	16.559(040)	17.152(038)	16.073(039)	16.077(043)
2016 May 01	57509.795	103.876	–	18.453(085)	16.666(047)	17.558(042)	16.402(040)	–
2016 May 02	57510.720	104.801	–	18.464(085)	16.815(044)	17.580(041)	16.376(041)	16.301(041)
2016 May 02	57510.835	104.916	–	18.445(063)	16.891(044)	17.529(060)	16.396(029)	–
2016 May 04	57512.030	106.111	–	18.284(093)	16.776(038)	17.391(035)	16.307(026)	16.240(034)
2016 May 04	57512.740	106.821	–	18.401(059)	16.806(040)	17.518(026)	16.417(040)	16.289(045)
2016 May 05	57513.710	107.791	–	18.292(065)	16.766(049)	17.424(037)	16.322(037)	16.273(043)
2016 May 10	57518.965	113.046	–	18.189(057)	16.871(055)	17.581(060)	16.459(042)	16.376(037)
2016 May 11	57519.935	114.016	–	18.307(069)	16.860(033)	17.364(034)	16.412(027)	16.398(040)
2016 May 12	57520.050	114.131	–	18.338(045)	16.900(041)	17.454(032)	16.431(029)	16.443(037)
2016 May 14	57522.935	117.016	–	18.500(112)	16.940(034)	–	–	–
2016 May 15	57523.123	117.204	–	18.468(115)	16.926(043)	17.485(038)	16.460(037)	16.388(040)
2016 May 20	57528.760	122.841	–	18.225(102)	17.089(061)	–	16.470(038)	16.397(033)
2016 May 28	57536.065	130.146	–	18.331(035)	17.056(037)	–	–	–
2016 Jun. 04	57543.760	137.841	–	–	17.416(188)	17.841(029)	16.780(032)	16.824(024)
2016 Jun. 05	57544.763	138.844	–	18.729(040)	17.372(042)	17.934(034)	16.859(028)	16.853(026)
2016 Jun. 06	57545.885	139.966	–	18.682(051)	17.466(033)	17.927(041)	16.883(031)	16.851(026)
2016 Jun. 07	57546.745	140.826	–	18.608(066)	17.489(038)	–	–	–
2016 Jun. 08	57547.715	141.796	–	18.734(054)	17.494(038)	17.931(031)	17.007(029)	16.870(041)
2016 Jun. 23	57562.705	156.786	–	18.484(060)	17.416(043)	17.855(041)	16.812(034)	–
2016 Jun. 24	57563.705	157.786	–	18.612(159)	17.516(101)	–	–	–
2016 July 06	57575.745	169.826	–	18.634(045)	17.668(045)	18.069(037)	16.871(034)	17.084(028)

[a]Relative to the explosion date, MJD = 57405.92.

the plateau phase (∼30–110) d, the $(U-B)_0$ and $(B-V)_0$ colours become progressively red by ∼1 mag as the cooling rate decreases, while $(V-R)_0$ and $(V-I)_0$ colours show little change. The $(B-V)_0$ colour shows a peak during the transitional phase around $t\sim+110$ d, which is also visible in other SNe IIP. In the nebular phase (>120 d), the $B-V$ colour becomes gradually bluer, similar to that of SN 1999em and SN 2014cx.

3.5 Bolometric light curve

Due to the lack of near-infrared observations, we calculated the quasi-bolometric luminosity of SN 2016X following the same method as described in Huang et al. (2015). After corrections for the line-of-sight extinction, the broad-band magnitudes were converted into fluxes at the effective wavelength when V-band observations were available. The data in other bands, if not obtained, were es-

Table 5. UV and optical photometry of SN 2016X from *Swift* (1σ uncertainties).

UT date (yy/mm/dd)	MJD	Phase[a] (d)	*uvw*2 (mag)	*uvm*2 (mag)	*uvw*1 (mag)	*U* (mag)	*B* (mag)	*V* (mag)
2016 Jan. 21	57408.07	2.15	12.74(03)	12.72(03)	12.91(03)	13.49(03)	14.83(04)	14.91(06)
2016 Jan. 22	57409.45	3.53	12.89(04)	12.75(04)	12.87(04)	13.25(04)	14.55(04)	14.74(06)
2016 Jan. 22	57409.79	3.87	12.82(04)	12.66(04)	12.80(04)	13.20(04)	14.49(04)	14.57(06)
2016 Jan. 23	57410.19	4.27	12.79(04)	12.62(04)	12.73(04)	13.11(04)	14.36(04)	14.47(06)
2016 Jan. 24	57411.82	5.90	13.00(04)	12.72(04)	12.72(04)	12.95(04)	14.24(04)	14.22(05)
2016 Jan. 25	57412.50	6.58	13.17(03)	12.86(03)	12.82(03)	13.00(03)	14.21(03)	14.21(05)
2016 Jan. 27	57414.25	8.33	13.55(04)	–	–	–	–	–
2016 Feb. 01	57419.03	13.11	14.57(05)	–	13.87(05)	13.28(04)	14.29(04)	14.13(05)
2016 Feb. 01	57419.76	13.84	14.76(06)	–	14.03(05)	13.36(04)	14.30(04)	14.18(05)
2016 Feb. 06	57424.69	18.77	16.11(20)	–	15.38(07)	14.05(05)	14.49(05)	–
2016 Feb. 07	57425.10	19.18	16.25(08)	16.43(08)	15.33(06)	14.06(04)	14.53(04)	14.28(05)
2016 Feb. 08	57426.63	20.71	16.60(09)	16.83(10)	15.67(07)	14.25(05)	14.69(05)	14.31(06)
2016 Feb. 09	57427.96	22.04	16.92(09)	17.12(09)	15.89(07)	14.55(05)	14.68(05)	14.27(05)
2016 Feb. 10	57428.39	22.47	16.89(10)	17.16(11)	15.92(08)	14.54(05)	14.72(05)	14.36(06)
2016 Feb. 17	57435.68	29.76	18.24(19)	18.66(26)	17.02(10)	15.59(07)	15.14(05)	14.48(06)
2016 Feb. 21	57439.80	33.88	18.54(18)	19.39(34)	17.21(11)	15.83(08)	15.26(05)	14.62(06)
2016 Feb. 23	57441.59	35.67	18.40(18)	18.91(26)	17.36(10)	16.10(08)	15.34(05)	14.71(07)
2016 Mar. 1	57448.77	42.85	18.75(22)	–	17.64(14)	16.29(09)	15.52(06)	14.81(07)
2016 Mar. 5	57452.46	46.54	18.95(22)	–	17.73(13)	16.39(09)	15.61(06)	14.80(06)

[a]Relative to the explosion date, MJD = 57405.92.

timated by interpolating the observations on adjacent nights. The spectral energy distributions (SEDs) were integrated, and the observed fluxes were converted to luminosity with the Tully–Fisher distance from Sorce et al. (2014).

Fig. 6 shows the quasi-bolometric UV+optical (*UBVRI*) light curve of SN 2016X, compared with that of some representative SNe IIP. The peak luminosity is estimated to be as log $L_{\rm bol}$ = 42.17 erg s^{-1}. Note that the calculations of the quasi-bolometric light curves still suffer large uncertainties in the distance modulus. The plateau luminosity of SN 2016X is not constant but shows a monotonic decline up to $t \sim 90$ d after explosion, which is similar with SN 2004et and SN 2013ej. The decline rate during the plateau phase is faster than other normal SNe IIP but comparable to the fast-declining type IIP SN 2013ej. The tail luminosity is lower than that of comparison SNe IIP except for the sub-luminous SN 2005cs, indicating that a relatively small amount of ^{56}Ni was synthesized in the explosion. Using the least-square fitting, the decline rate at the nebular phase is estimated to be 0.6 mag (100 d)$^{-1}$.

For the bolometric luminosity, the UV flux has a significant contribution in the early time ($\leq$ 30 d), as shown in Fig. 7. The UV contribution can reach $\gtrsim$30 per cent for SN 2016X, which is much higher than other comparison SNe IIP (i.e. ∼15 per cent). Prominent UV emission is also in agreement with the higher temperature and larger progenitor radius derived for SN 2016X in Section 5.2. After about one month, the UV contribution becomes marginally important for most SNe IIP when entering into the plateau phase. Note that the above calculations of UV fraction may suffer from the uncertainties in dust extinctions applied for different SNe IIP.

4 SPECTROSCOPIC ANALYSIS

4.1 Evolution of optical spectra

A total of 40 optical spectra of SN 2016X covering the phase from +2 to +140 d after the explosion are displayed in Fig. 8. The phases marked in the plot are relative to the explosion date estimated in Section 3.1. All spectra have been corrected for the recession velocity of the host galaxy (1321 ± 2 km s^{-1}).[4] The main spectral features are identified in previous studies for SNe IIP (Leonard et al. 2002; Pastorello et al. 2004), and are also marked in Fig. 9.

The first spectrum, taken at less than 2 d after explosion, shows a featureless blue continuum, consistent with a very young event of core-collapse explosion. The blue continuum indicates that the photosphere has a temperature that is above 10^4 K. At $t \approx 2.6$ d, shallow hydrogen Balmer lines, and He I λ5876 lines with broad P-Cygni profiles, become visible. The blue wing of Hα absorption indicates that the expansion velocity can reach up to ∼18 000 km s^{-1}. A double P-Cygni absorption of Hα appears in the t = +8 d spectrum (see Fig 9a), and disappears after one month since explosion. The high-velocity feature is also reported in other SNe IIP, which might be due to Si II λ6355.

After two weeks since explosion ($t \geq 15$ d), the He I feature vanishes and is replaced by Na I line at the similar position. Apart from hydrogen Balmer lines, O I λ7774, Ca II H & K (λλ 3934, 3968), Ca II NIR triplet (λλ 8498, 8542, 8662), and Fe II multiplets are also clearly seen in the spectra. During the photospheric phase, the spectra turn progressively redder, and a number of narrow metal lines (Fe II, Ti II, Sc II, Ba II, Mg II, etc.) emerge in the spectra. These features grow progressively stronger and dominate the spectra over time.

After ∼90 d, the continuum flattens, and the spectra become dominated by emission lines, meaning that the SN enters into the nebular phase. The Hα emission profile shows a weak asymmetric feature (also seen in Fig. 9c). The asymmetric feature has been commonly observed in a few SNe IIP (i.e. SNe 1999em, 2004dj, and 2013ej), and might result from interaction with circumstellar medium, asymmetry in the line-emitting region (Leonard et al. 2002), or bipolar ^{56}Ni distribution in a spherical envelope (Chugai 2006). The subsequent spectra show permitted lines due to metals,

[4] http://leda.univ-lyon1.fr/

Table 6. Observing log for optical spectra of SN 2016X.

UT date	MJD	Phase[a] (d)	Range (Å)	Exposure (s)	Telescope + Instrument
2016 Jan. 20	57407.74	1.82	3300–9000	900	LCO 2.0 m Telescope South + FLOYDS
2016 Jan. 21	57408.52	2.60	3300–10 000	900	LCO 2.0 m Telescope North + FLOYDS
2016 Jan. 23	57410.48	4.56	3250–10 000	900	LCO 2.0 m Telescope North + FLOYDS
2016 Jan. 23	57410.68	4.76	3250–10 000	900	LCO 2.0 m Telescope South + FLOYDS
2016 Jan. 23	57410.89	4.97	3500–9000	1500	Lijiang 2.4 m + YFOSC
2016 Jan. 25	57412.47	6.55	3250–10 000	900	LCO 2.0 m Telescope North + FLOYDS
2016 Jan. 25	57412.67	6.75	3250–10 000	900	LCO 2.0 m Telescope South + FLOYDS
2016 Jan. 27	57414.52	8.60	3250–10 000	900	LCO 2.0 m Telescope North + FLOYDS
2016 Jan. 28	57415.54	9.62	3250–10 000	1200	LCO 2.0 m Telescope North + FLOYDS
2016 Jan. 28	57415.93	10.01	3500–9100	1200	Lijiang 2.4 m + YFOSC
2016 Jan. 31	57418.73	12.81	3350–10 000	1200	LCO 2.0 m Telescope South + FLOYDS
2016 Feb. 2	57420.88	14.96	3500–9100	1800	Lijiang 2.4 m + YFOSC
2016 Feb. 3	57421.46	15.54	3250–10 000	1200	LCO 2.0 m Telescope North + FLOYDS
2016 Feb. 6	57424.71	18.79	3400–10 000	1200	LCO 2.0 m Telescope South + FLOYDS
2016 Feb. 10	57428.68	22.76	3400–10 000	1200	LCO 2.0 m Telescope South + FLOYDS
2016 Feb. 13	57431.90	25.98	3500–9100	1500	Lijiang 2.4 m + YFOSC
2016 Feb. 16	57434.69	28.77	3550–10 000	1200	LCO 2.0 m Telescope South + FLOYDS
2016 Feb. 16	57434.86	28.94	3500–9100	1500	Lijiang 2.4 m + YFOSC
2016 Feb. 18	57436.87	30.95	3500–9100	1500	Lijiang 2.4 m + YFOSC
2016 Feb. 22	57440.47	34.55	3550–10 000	1200	LCO 2.0 m Telescope North + FLOYDS
2016 Feb. 23	57441.84	35.92	3500–9100	1500	Lijiang 2.4 m + YFOSC
2016 Feb. 28	57446.54	40.62	3500–10 000	1200	LCO 2.0 m Telescope North + FLOYDS
2016 Feb. 28	57446.84	40.92	3500–9100	1500	Lijiang 2.4 m + YFOSC
2016 Mar. 6	57453.64	47.72	3500–10 000	1200	LCO 2.0 m Telescope North + FLOYDS
2016 Mar. 11	57458.86	52.94	3500–9100	1800	Lijiang 2.4 m + YFOSC
2016 Mar. 12	57459.69	53.77	3700–10 000	1200	LCO 2.0 m Telescope South + FLOYDS
2016 Mar. 18	57465.51	59.59	3600–10 000	1200	LCO 2.0 m Telescope North + FLOYDS
2016 Mar. 18	57465.75	59.83	3500–9100	1800	Lijiang 2.4 m + YFOSC
2016 Mar. 21	57468.74	62.82	3950–10 000	1200	LCO 2.0 m Telescope South + FLOYDS
2016 Mar. 27	57474.71	68.79	3700–9150	2850	Lijiang 2.4 m + YFOSC
2016 Apr. 4	57482.72	76.80	3650–9150	2100	Lijiang 2.4 m + YFOSC
2016 Apr. 7	57485.51	79.59	3800–10 000	1200	LCO 2.0 m Telescope South + FLOYDS
2016 Apr. 13	57491.69	85.77	3900–10 000	1200	LCO 2.0 m Telescope South + FLOYDS
2016 Apr. 17	57495.69	89.77	3900–8780	2100	Xinglong 2.16 m + BFOSC
2016 Apr. 17	57495.80	89.88	3600–9100	2100	Lijiang 2.4 m + YFOSC
2016 Apr. 26	57504.72	98.80	3600–9100	2100	Lijiang 2.4 m + YFOSC
2016 Apr. 29	57507.26	101.34	3500–10 000	1200	LCO 2.0 m Telescope North + FLOYDS
2016 May 2	57510.72	104.80	3500–9170	2100	Lijiang 2.4 m + YFOSC
2016 May 21	57529.27	123.35	4500–9300	1800	LCO 2.0 m Telescope North + FLOYDS
2016 Jun. 9	57548.34	142.42	3500–10 000	3600	LCO 2.0 m Telescope North + FLOYDS

[a]Relative to the explosion date, MJD = 57405.92.

when the outer ejecta became optically thin. And the spectra are characterized by the presence of forbidden lines [O I] λλ6300, 6364 and [Ca II] λλ7291, 7324.

4.2 Comparison with other SNe IIP

In Fig. 9, we compare the spectra evolution of SN 2016X to a few other SNe IIP at similar phases, i.e. the early phase at 1 week, the plateau phase at 2 months, and the nebular phase at 4 months after explosion. SN 2016X shows similarities with these comparison SNe IIP (especially SN 2013ej and SN 2014cx) in the spectral evolution. In the early phase, the spectrum of SN 2016X shows weaker and broader profiles of Balmer lines and He I line compared to SN 1999em and SN 2005cs. During the plateau phase, the spectra of SN 2016X and the comparison objects are dominated by metal lines, including Fe II, Ti II, Sc II, Ba II, and Mg II. The forbidden lines such as [O I] and [Ca II] emerge in the spectra when the SNe enter into the nebular phase. In comparison, SN 2005cs shows much narrower absorption features and redder continuum at this phase.

4.3 Expansion velocities

The measurement of the ejecta velocities and comparison with that of other SNe IIP are presented in this subsection. The expansion velocities of hydrogen and metal lines are measured by using *splot* in IRAF to locate the absorption minima. The upper panel of Fig. 10 shows the line velocities of Hα, Hβ, and Fe II λλ 5169, 5018, and 4924. During the first week after the explosion, the expansion velocity of hydrogen is above 10 000 km s^{-1} and it declines very rapidly. Later on, the velocity then declines in an exponential trend over time. The velocity of Fe II lines, which is a good indicator of photospheric velocity, is always lower than that of hydrogen lines and it decreases below 3000 km s^{-1} after 90 d. This can be explained by that the Fe II lines are formed in the inner layers with larger optical depths.

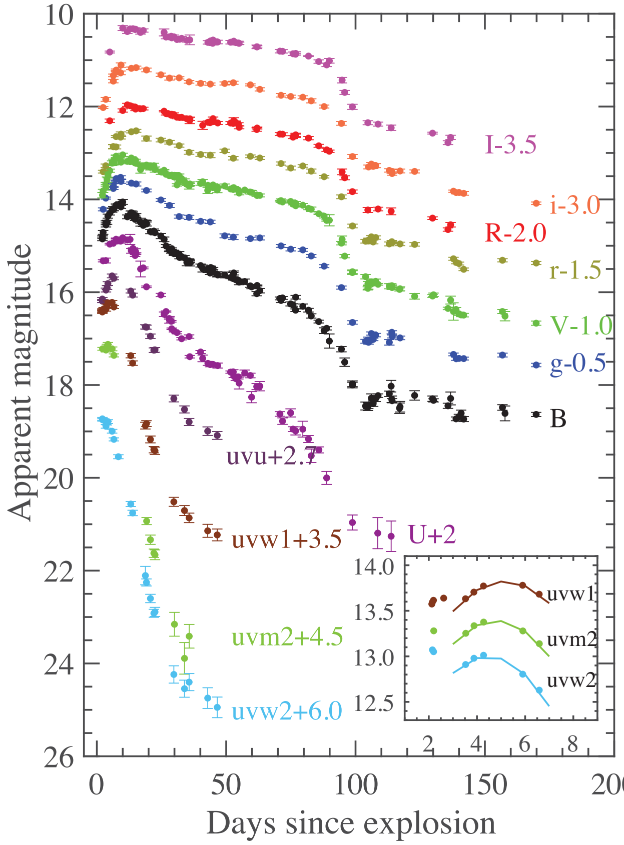

Figure 2. Light curves of SN 2016X in UV and optical bands. The insert is a zoom on the early-time UV light curve, with polynomial fitting to the data around maximum. Prominent UV emission is clearly seen at a few days before the primary UV peaks. The phase is given relative to the estimated explosion date, MJD = 57405.92.

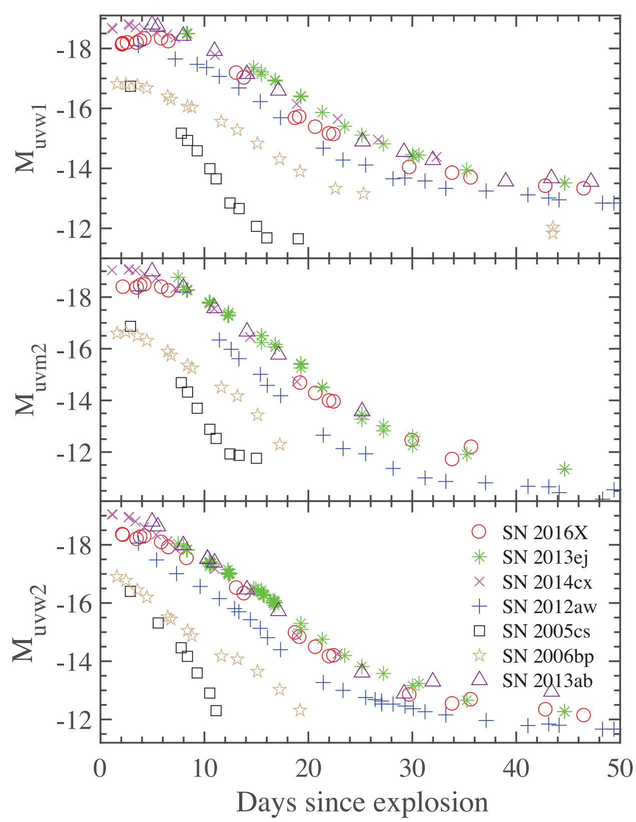

Figure 3. Comparison of the UV absolute light curves of SN 2016X with a few well-observed SNe IIP. For the comparison SNe, the distance modulus μ in mag and extinction A_V in mag are listed in the brackets after the name of each SN sample, and the references are: SN 2005cs (29.26, 0.095), Brown et al. (2007), Pastorello et al. (2009); SN 2006bp (31.22, 0.08), Immler et al. (2007); SN 2012aw (29.98, 0.08), Bayless et al. (2013); SN 2013ab (31.90, 0.14), Bose et al. (2015); SN 2013ej (29.91, 0.19), Huang et al. (2015); SN 2014cx (31.74, 0.31), Huang et al. (2016).

In the lower panel of Fig. 10, we compare the velocity evolution of Fe λ5169 between SN 2016X and other SNe IIP. It is obvious that the velocity of SN 2016X is higher than SN 1999em (by ∼1000 km s^{-1}) and SN 2005cs (by ∼3000 km s^{-1}), and close to SN 2013ej, SN 2004et, and SN 2014cx.

5 DISCUSSION

5.1 Nickel mass

The amount of ^{56}Ni synthesized in the explosion of SNe IIP can be estimated by the luminosity of their late-time light curves. In the nebular phase, the light curve is powered by the radioactive decay of ^{56}Ni to ^{56}Co and ^{56}Co to ^{56}Fe, with *e*-folding time of 8.8 and 111.26 d, respectively. The mass of ^{56}Ni of SN 1987A has been accurately determined to be 0.075 ± 0.005 M$_\odot$ (Arnett 1996). We adopt a linear least square fit to the nebular luminosity during the phase 120–160 d, and obtain L(SN 2016X)/L(SN 1987A) = 0.43 at 140 d, from which we derive $M(^{56}\mathrm{Ni}) = 0.032 \pm 0.006$ M$_\odot$.

Assuming that the γ photons produced from the ^{56}Ni to ^{56}Fe are fully thermalized, the ^{56}Ni mass can be also estimated from the tail luminosity. Using equation 2 in Hamuy (2003), we estimate the ^{56}Ni mass to be $M(^{56}\mathrm{Ni}) = 0.034 \pm 0.005$ M$_\odot$.

Elmhamdi, Chugai & Danziger (2003) found a tight correlation between the ^{56}Ni mass and a steepness parameter of the *V*-band light curve at the transitional phase. For SN 2016X, we fit the *V*-band light curve and estimate the steepness parameter *S* as 0.099 mag d^{-1} at the epoch of inflection t_i = 92 d. Using the empirical relation [$\log M(^{56}\mathrm{Ni}) = -6.2295\, S - 0.8147$], the mass of ^{56}Ni for SN 2016X is estimated to be 0.037 ± 0.003 M$_\odot$. This value is consistent with that derived from the tail luminosity. Therefore, the average value of ^{56}Ni mass is taken as 0.034 ± 0.006 M$_\odot$.

5.2 Properties of progenitor

For CC SNe, shortly after the shock breakout, the shock-heated stellar envelope cools down due to the outward expansion. The time-scale of cooling depends mainly on the initial radius of the progenitor, opacity, and gas composition. And the early light curves of SNe are dominated by the radiation from the expanding envelope. Some simple analytic expressions have been developed to describe the properties of the emitted radiation and are used to constrain the progenitor radius (e.g. Chevalier & Irwin 2011; Rabinak & Waxman 2011; Sapir & Waxman 2017). For example, progenitors with larger radius (i.e. RSG with 500–1000 R$_\odot$) stay at higher temperature and cool down at a slower pace than those with smaller radius (i.e. BSG with 50–100 R$_\odot$), as indicated by the expression $T_{\mathrm{ph}}(t) = 1.6\, f_\rho^{-0.037} \frac{E_{51}^{0.027} R_{*,13}^{1/4}}{(M/\mathrm{M}_\odot)^{0.054} \kappa_{0.34}^{0.28}} t_5^{-0.45}$ eV, where

Table 7. Photometric parameters of SN 2016X.

	U (mag)	B (mag)	g (mag)	V (mag)	r (mag)	R (mag)	i (mag)	I (mag)
Peak magnitude	13.25	14.14	14.04	14.05	13.99	13.91	14.07	13.77
Phase of maximum[a]	9.26	9.60	10.60	11.26	13.70	13.76	13.55	14.11
Plateau magnitude	–	–	15.31	14.67	14.60	14.46	14.50	14.07
Decay rate (mag/100 d)	–	0.58	0.99	1.35	1.25	1.22	1.05	1.14

[a] Relative to the explosion date, MJD = 57405.92.

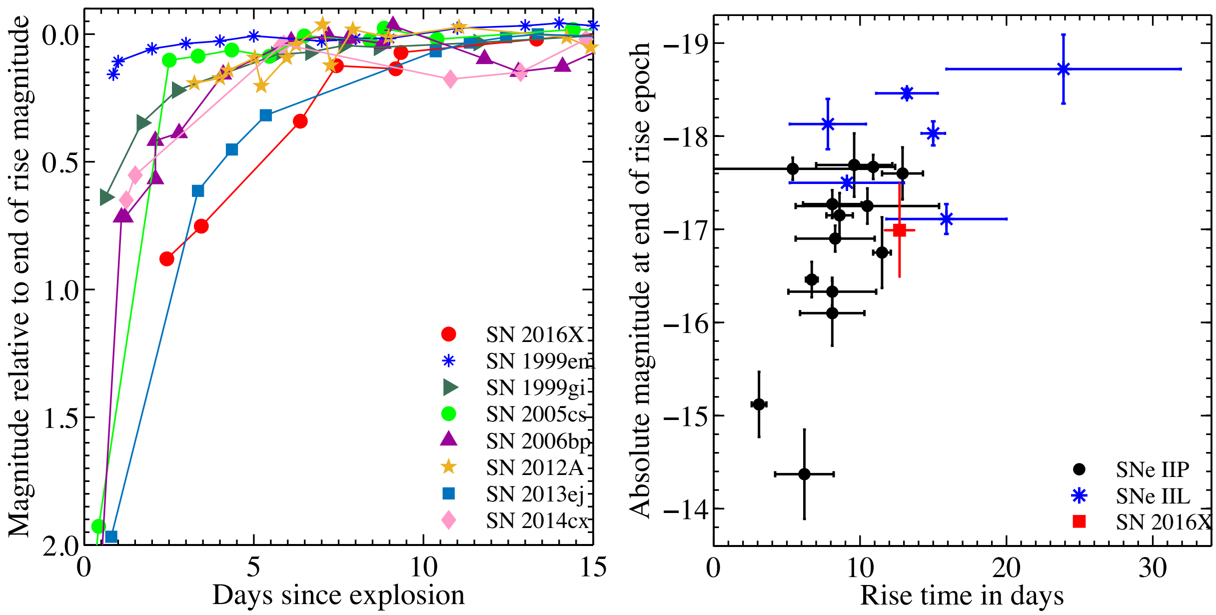

Figure 4. Left: comparison of the *r*/*R*-band light curve of SN 2016X with a few SNe IIP. Right: comparison of *r*/*R*-band absolute magnitudes at the end-of-rise epoch and rise time. The filled red square represents SN 2016X while other dots represent a sample of SNe II from Gall et al. (2015).

f_ρ represents density profile, E_{51} is the energy in units of 10^{51} erg, $R_{*,\,13}$ is the radius in units of 10^{13} cm, $\kappa_{0.34}$ is the opacity in units of 0.34 cm^2 g^{-1}, and t_5 is time in units of 10^5 s.

Thanks to the timely follow-up observations from the *Swift* UVOT, we are able to better construct the SED and estimate the corresponding blackbody temperature (cooling phase of the shock breakout) for SN 2016X in the early phase. This allows us to constrain its progenitor radius by fitting to the temperature evolution. Adopting an optical opacity of 0.34 cm^2 g^{-1} and an RSG density profile $f_\rho = 0.13$ in the equation 13 from Rabinak & Waxman (2011), we yield an initial radius of 860–990 R$_\odot$ for the progenitor of SN 2016X, as shown in Fig. 11. We also overplot the temperature evolution and the best-fitting progenitor radius for SN 1987A, SN 2006bp, SN 2013ej, and SN 2014cx. One can see that SN 2016X has an apparently large progenitor in comparison with other SNe IIP.

Using the SuperNova Explosion Code (SNEC; Morozova et al. 2015), Morozova et al. (2016) find that the early properties of the light curves of SNe IIP depend sensitively on the radius of the progenitor star, with a relationship between the g-band rise time and the radius at the time of explosion [i.e. log R(R$_\odot$) = 1.225 log $t_{\rm rise}$ (d) + 1.692]. We also use this relation to estimate the size of the progenitor star. For SN 2016X, the g-band rise time is estimated as 10.60 ± 0.40 d, which leads to an estimate of 890 ± 40 R$_\odot$ for the progenitor of SN 2016X. This analysis, together with the result from shock breakout cooling, favours that SN 2016X has a larger progenitor with a radius up to ∼900–1000 R$_\odot$.

Based on the RSG sample in the Milky Way and Magellanic Clouds (MC; Levesque et al. 2005, 2006), González-Gaitán et al. (2015) found that there is a general tendency that the more massive RSG stars have larger radius sizes. A tight mass–radius relation can be obtained for the RSG stars in the Milky Way, i.e. R/R$_\odot$ = 1.4(M/M$_\odot$)$^{2.2}$, as shown in Fig. 12 (see the dashed line). This relation gives a rough estimate of 18.5–19.7 M$_\odot$ for the progenitor of SN 2016X, which is close to the 19 M$_\odot$ upper limit estimated by Dwarkadas (2014). In this plot, we also show the progenitor mass and radius estimated from photospheric cooling/hydrodynamic analysis and *Hubble Space Telescope* (*HST*) archive images for a sample of SNe IIP. We notice that mass and radius of these SNe IIP seem to follow that of the Galactic or MC RSGs, except that the hydrodynamic method gives a larger mass and a smaller radius for SN 2012aw. Table 8 lists the details of these estimates and the references. For a comparison, we overplot the mass–radius relation derived from RSGs in the MCs (see the

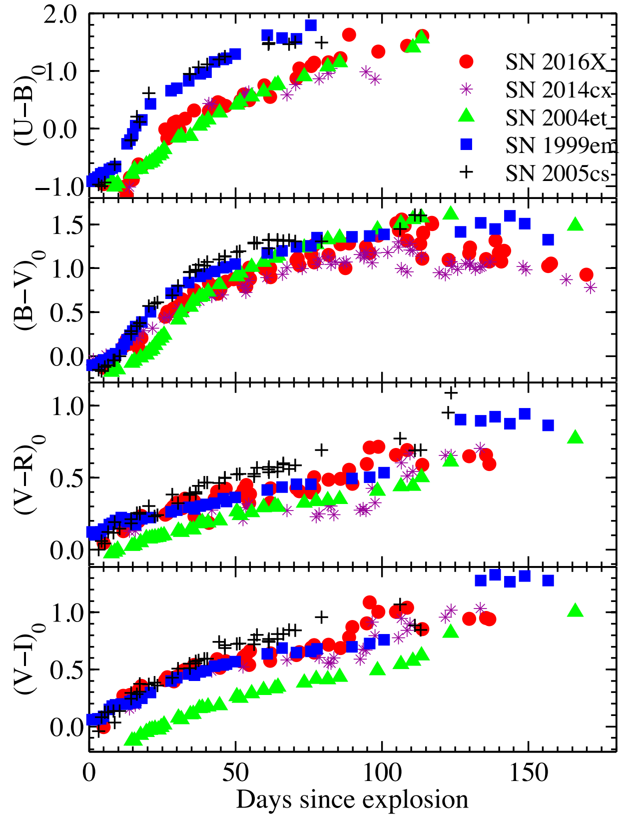

Figure 5. The colour-curve evolution of SN 2016X, along with that of other well-studied SNe IIP (SNe 1999em, 2004et, 2005cs, and 2014cx). All the colours have been corrected for both the Galactic and host-galaxy reddening.

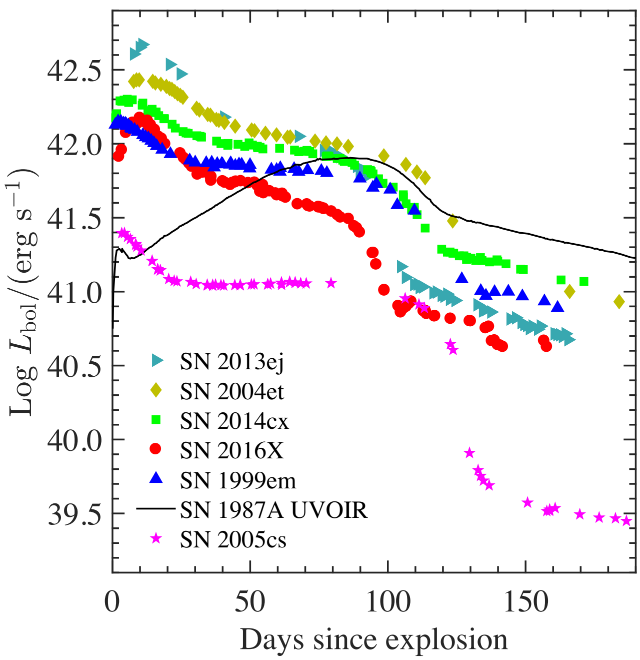

Figure 6. The quasi-bolometric light curve of SN 2016X compared with that of a few well-studied SNe IIP.

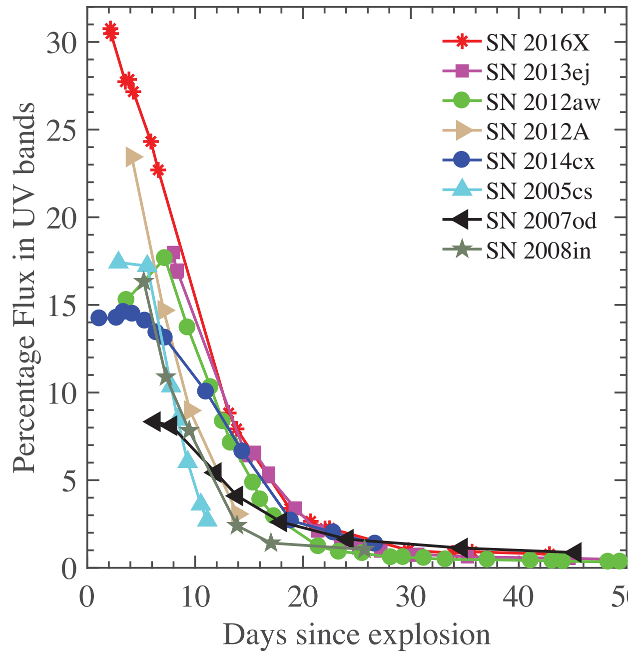

Figure 7. Temporal evolution of the UV contribution of SN 2016X in the first two months, compared with some well-studied SNe IIP (including SNe 2005cs, 2007od, 2008in, 2012A, 2012aw, 2013ej, and 2014cx). The comparison data are extracted from SOUSA.

dotted line). Given a radius, the star will have a larger mass for lower metallicity. This can be explained with that more metal-poor stars usually lose their mass at a lower efficiency.

As the host galaxy of SN 2016X UGC 08041 is a late-type Sd galaxy and the SN locates at its outskirts, it is possible that the progenitor of SN 2016X has a relatively lower metallicity. Considering this effect and hence the possible mass-loss of the progenitor star before the explosion, the mass range we derived for the progenitor of SN 2016X should be a lower limit. Along with SN 2012aw and SN 2012ec, the high mass derived for the progenitor of SN 2016X indicates that RSGs with an initial mass around or above 20.0 $M_\odot$ could lead to an explosion of a type IIP SN.

6 SUMMARY

In this paper, we present the UV/optical photometry and low-resolution spectroscopic observations for the type IIP SN 2016X up to 180 d after explosion. The high-quality UV/optical data allow us to place interesting constraints on the observational properties of SN 2016X and its progenitor. A brief summary of our results is listed below.

The *Swift* UVOT data reveal the presence of prominent UV emissions at just only 2 d before the primary UV peaks, which is very likely related to the shock breakout of very massive stars. For SN 2016X, the UV contribution to the total flux can reach $\gtrsim$30 per cent for SN 2016X in the early phase, while the typical value is $\sim$15 per cent. In particular, this SN is found to have a very long rise time before reaching the maximum light, i.e. 12.6 $\pm$ 0.5 d in the *R* band, in contrast to $\sim$7.0 d for normal SNe IIP. The photometric and spectral evolution is overall similar to SN 2013ej.

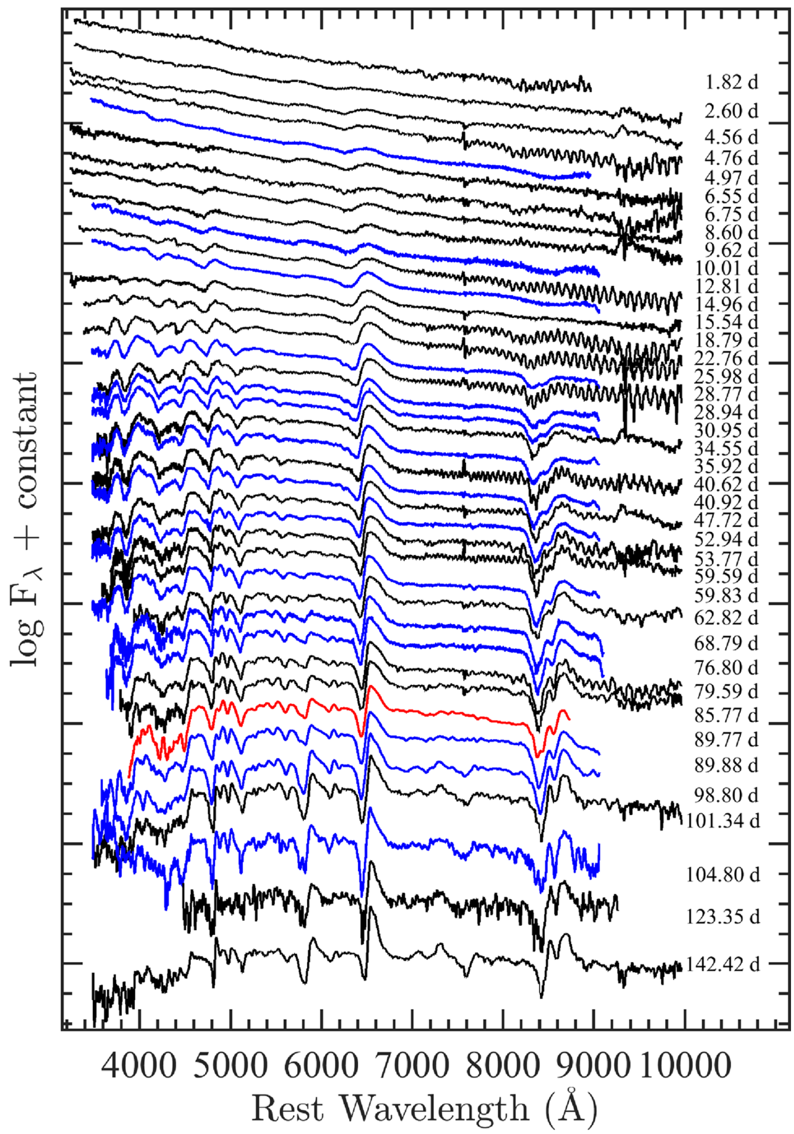

Figure 8. The spectra sequence of SN 2016X. The spectra obtained with the LCO, LJ 2.4-m telescope, and the Xinglong 2.16-m telescope are shown in black, blue, and red curves, respectively. The phase relative to the explosion date (MJD = 57405.92) is shown on the right of each spectrum.

Using the early-time temperature evolution inferred from the *Swift* UV photometry, we derived an initial radius of 860–990 $R_\odot$ for the progenitor of SN 2016X. The long *g*-band rise time of SN 2016X also indicates a large progenitor radius of ∼890 $R_\odot$ according to the rise time–radius relation from the SNEC. Based on the mass–radius relation of the Galactic RSG, we also obtain a rough mass estimate of 18.5–19.7 $M_\odot$ for the progenitor of SN 2016X, which provides further evidence that massive stars with an initial mass up to 19–20 $M_\odot$could also produce an explosion of a type IIP SN.

ACKNOWLEDGEMENTS

We acknowledge the support of the staff of the Lijiang 2.4-m and Xinglong 2.16-m telescope. Funding for the LJT has been provided by Chinese Academy of Sciences and the People's Government of Yunnan Province. The LJT is jointly operated and administrated by Yunnan Observatories and Centre for Astronomical Mega-Science, CAS. This work is supported by the National Natural Science Foundation of China (NSFC grants 11178003, 11325313, and 11633002). This work was also partially supported by the Collaborating Research Program (OP201702) of the Key Laboratory of the Structure and Evolution of Celestial Objects, Chinese Academy of Sciences. This work makes use of observations from LCO. DAH, CM, and GH are supported by the US NSF grant 1313484. Support for IA was provided by NASA through the Einstein Fellowship Program, grant PF6-170148. The work made use of *Swift*/UVOT data reduced by PJB and released in the SOUSA. SOUSA is supported by NASA's Astrophysics Data Analysis Program through grant NNX13AF35G. JJZ is supported by the NSFC (grants 11403096 and 11773067), the Key Research Program of the CAS (Grant no. KJZD-EW- M06), the Youth Innovation Promotion Association of the CAS, and the CAS 'Light of West China' Program. TMZ is supported by the NSFC (grants 11203034).

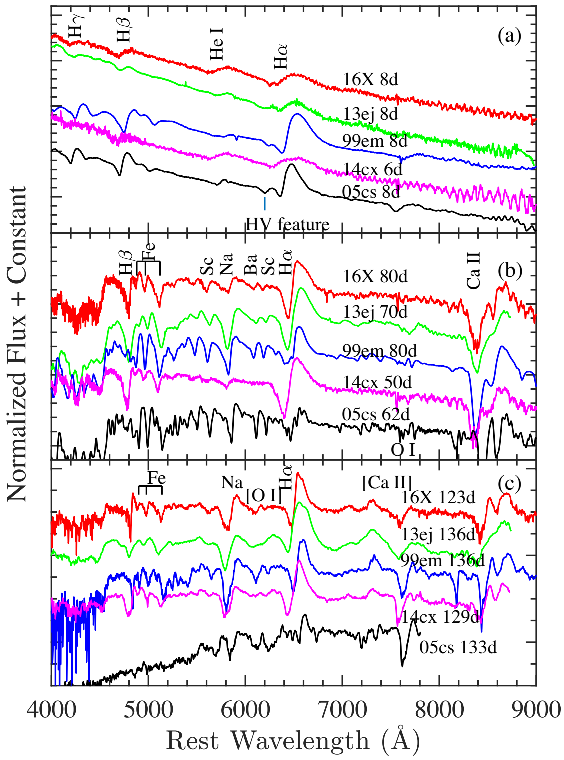

Figure 9. Spectral comparison of SN 2016X with those of other well-studied SNe IIP at early (1 week), plateau (80 d), and nebular (130 d) phases.

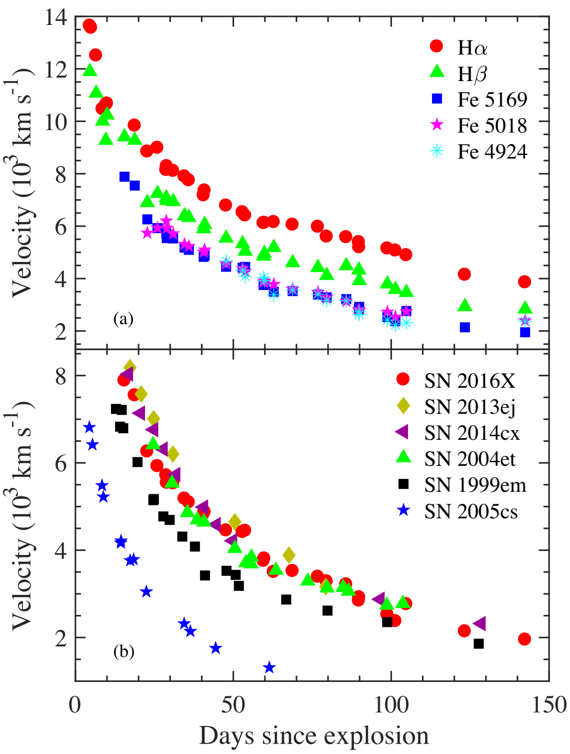

Figure 10. Upper: the velocity evolution of H α H β and Fe II lines. Lower: comparison of evolution of photospheric velocity (measured by Fe λ5169) of SN 2016X with some well-studied type II-P SNe such as SN 1999em (Leonard et al. 2002), SN 2004et (Sahu et al. 2006), SN 2005cs (Pastorello et al. 2009), SN 2013ej (Huang et al. 2015), and SN 2014cx (Huang et al. 2016).

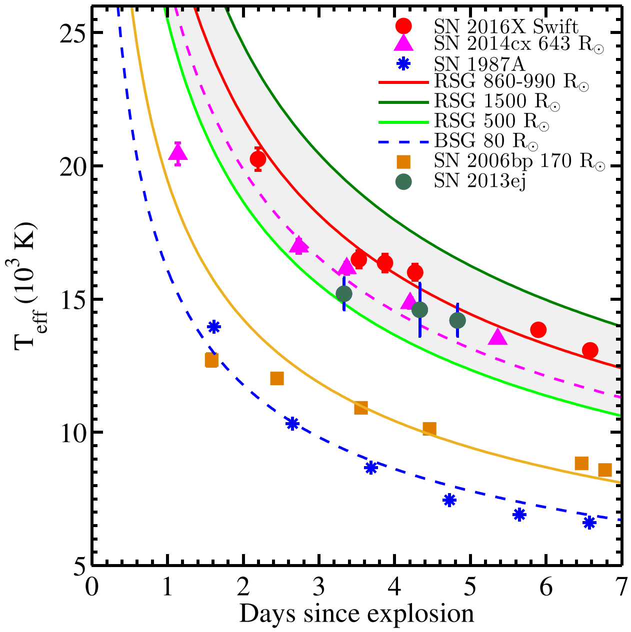

Figure 11. Radius estimates using the prescription from Rabinak & Waxman (2011). The best fit for SN 2016X is 860–990 $R_{\odot}$. Overplotted are the comparison objects SN 1987A, 2006bp, 2013ej, and 2014cx (Valenti et al. 2014; Huang et al. 2016).

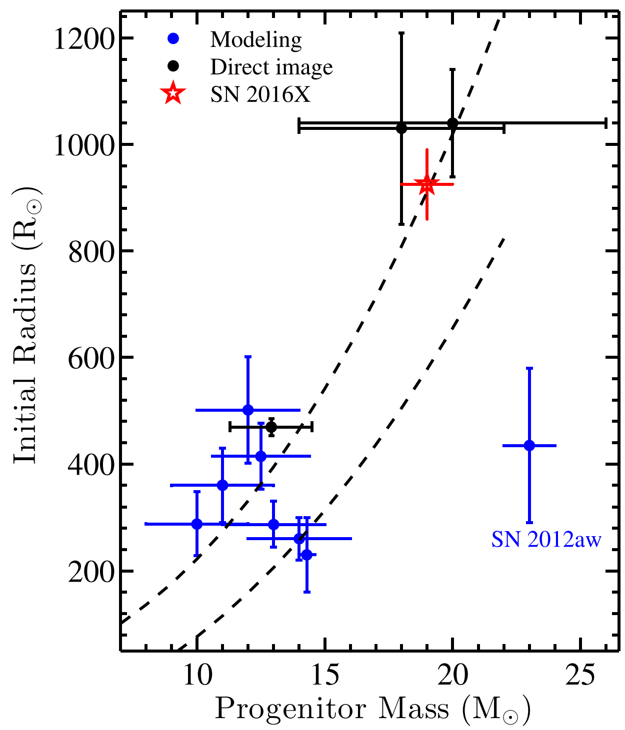

Figure 12. The progenitor mass and radius for a sample of SNe IIP. The blue dots represent the estimates using hydrodynamic modelling, while the black dots are results from analysis of the pre-explosion images (see the reference from Table 8). Dashed lines represent the mass–radius relation derived from the Galactic (upper) and MC (lower) RSGs, respectively (González-Gaitán et al. 2015).

Table 8. The mass and radius of SNe IIP using direct archive images and hydrodynamic model method.

SN name	*HST* image		Modelling		References
	mass ($M_\odot$)	radius ($R_\odot$)	mass ($M_\odot$)	radius ($R_\odot$)	
SN 2005cs	9^{+3}_{-2}	–	11	360 ± 70	Maund, Smartt & Danziger (2005); Pumo et al. (2017)
SN 2008bk	$12.9^{+1.6}_{-1.8}$	470 ± 16	12	502	Maund et al. (2014); Lisakov et al. (2017)
SN 2009N	–	–	13 ± 2	287 ± 43	Takáts et al. (2014)
SN 2009md	$8.5^{+6.5}_{-1.5}$	–	10	288	Fraser et al. (2011); Pumo et al. (2017)
SN 2012A	$10.5^{+4.5}_{-2}$	–	14 ± 2	260 ± 40	Tomasella et al. (2013)
SN 2012aw	14–26	1040 ± 100	22–24	290–580	Van Dyk et al. (2012); Fraser et al. (2012); Dall'Ora et al. (2014)
SN 2012ec	14–22	1030 ± 180	14.0–14.6	230 ± 70	Maund et al. (2013); Barbarino et al. (2015)
SN 2013ej	8–15.6	–	12.5 ± 1.9	415 ± 62	Fraser et al. (2014); Huang et al. (2015)
SN 2016X	–	–	18.5–19.7	925 ± 65	this work

REFERENCES

Ahn C. P. et al., 2012, ApJS, 203, 21
Anderson J. P. et al., 2014, ApJ, 786, 67
Arnett D., 1996, Supernovae and Nucleosynthesis: An Investigation of the History of Matter, from the Big Bang to the Present. Princeton Univ. Press, Princeton
Barbarino C. et al., 2015, MNRAS, 448, 2312
Barbon R., Ciatti F., Rosino L., 1979, A&A, 72, 287
Bayless A. J. et al., 2013, ApJ, 764, L13
Bock G., Shappee B. J., Stanek K. Z. et al., 2016, Astron. Telegram, 8566
Bose S., Valenti S., Misra K. et al., 2015, MNRAS, 450, 2373
Breeveld A. A., Landsman W., Holland S. T., Roming P., Kuin N. P. M., Page M. J., 2011, in McEnery J. E., Racusin J. L., Gehrels N., eds, AIP Conf. Proc. Vol. 1358, Gamma Ray Bursts 2010. Am. Inst. Phys., New York, p. 373
Brown P. J. et al., 2007, ApJ, 659, 1488
Brown P. J. et al., 2009, AJ, 137, 4517
Brown T. M. et al., 2013, PASP, 125, 1031
Brown P. J., Breeveld A. A., Holland S., Kuin P., Pritchard T., 2014, Ap&SS, 354, 89
Brown P. J., Breeveld A., Roming P. W. A., Siegel M., 2016, AJ, 152, 102
Chevalier R. A., Irwin C. M., 2011, ApJ, 729, L6
Chonis T. S., Gaskell C. M., 2008, AJ, 135, 264
Chugai N. N., 2006, Astron. Lett., 32, 739
Dall'Ora M. et al., 2014, ApJ, 787, 139
Dwarkadas V. V., 2014, MNRAS, 440, 1917
Ekström S. et al., 2012, A&A, 537, A146
Elmhamdi A., Chugai N. N., Danziger I. J., 2003, A&A, 404, 1077
Falk S. W., Arnett W. D., 1977, ApJS, 33, 515
Fan Z. et al., 2016, PASP, 128, 115005
Fan Y.-F., Bai J.-M., Zhang J.-J., Wang C.-J., Chang L., Xin Y.-X., Zhang R.-L., 2015, Res. Astron. Astrophys., 15, 918
Faran T. et al., 2014, MNRAS, 445, 554
Filippenko A. V., 1997, ARA&A, 35, 309
Fraser M. et al., 2011, MNRAS, 417, 1417
Fraser M. et al., 2012, ApJ, 759, L13
Fraser M. et al., 2014, MNRAS, 439, L56
Gal-Yam A. et al., 2011, ApJ, 736, 159
Gall E. E. E. et al., 2015, A&A, 582, A3
Gehrels N. et al., 2004, ApJ, 611, 1005
Gezari S. et al., 2008, ApJ, 683, L131
González-Gaitán S. et al., 2015, MNRAS, 451, 2212
Grasberg E. K., Nadezhin D. K., 1976, Ap&SS, 44, 409
Grassberg E. K., Imshennik V. S., Nadyozhin D. K., 1971, Ap&SS, 10, 28
Grupe D. et al., 2016, Astron. Telegram, 8588
Hamuy M., 2003, ApJ, 582, 905
Horne K., 1986, PASP, 98, 609
Hosseinzadeh G., Arcavi I., McCully C., Howell D. A., Sand D., Valenti S., 2016, Astron. Telegram, 8567
Huang F., Li J.-Z., Wang X.-F., Shang R.-C., Zhang T.-M., Hu J.-Y., Qiu Y.-L., Jiang X.-J., 2012, Res. Astron. Astrophys., 12, 1585
Huang F. et al., 2015, ApJ, 807, 59
Huang F. et al., 2016, ApJ, 832, 139
Ibeling D., Heger A., 2013, ApJ, 765, L43
Immler S. et al., 2007, ApJ, 664, 435
Inserra C. et al., 2011, MNRAS, 417, 261
Inserra C. et al., 2012, MNRAS, 422, 1122
Inserra C. et al., 2013, A&A, 555, A142
Jerkstrand A., Fransson C., Maguire K., Smartt S., Ergon M., Spyromilio J., 2012, A&A, 546, A28
Kasen D., Woosley S. E., 2009, ApJ, 703, 2205
Klein R. I., Chevalier R. A., 1978, ApJ, 223, L109
Landolt A. U., 1992, AJ, 104, 340
Leonard D. C. et al., 2002, PASP, 114, 35
Levesque E. M., Massey P., Olsen K. A. G., Plez B., Josselin E., Maeder A., Meynet G., 2005, ApJ, 628, 973
Levesque E. M., Massey P., Olsen K. A. G., Plez B., Meynet G., Maeder A., 2006, ApJ, 645, 1102
Li W. et al., 2011, MNRAS, 412, 1441
Lisakov S. M., Dessart L., Hillier D. J., Waldman R., Livne E., 2017, MNRAS, 466, 34
Maund J. R., Smartt S. J., Danziger I. J., 2005, MNRAS, 364, L33
Maund J. R. et al., 2013, MNRAS, 431, L102
Maund J. R., Mattila S., Ramirez-Ruiz E., Eldridge J. J., 2014, MNRAS, 438, 1577
Morozova V., Piro A. L., Renzo M., Ott C. D., Clausen D., Couch S. M., Ellis J., Roberts L. F., 2015, ApJ, 814, 63
Morozova V., Piro A. L., Renzo M., Ott C. D., 2016, ApJ, 829, 109
Nomoto K., 1984, ApJ, 277, 791
Nomoto K., Hashimoto M., 1988, Phys. Rep., 163, 13
Olivares E. F. et al., 2010, ApJ, 715, 833
Pastorello A. et al., 2004, MNRAS, 347, 74
Pastorello A. et al., 2009, MNRAS, 394, 2266
Patat F., Barbon R., Cappellaro E., Turatto M., 1994, A&A, 282, 731
Pumo M. L., Zampieri L., 2011, ApJ, 741, 41
Pumo M. L., Zampieri L., Spiro S., Pastorello A., Benetti S., Cappellaro E., Manicò G., Turatto M., 2017, MNRAS, 464, 3013
Rabinak I., Waxman E., 2011, ApJ, 728, 63
Roming P. W. A. et al., 2005, Space Sci. Rev., 120, 95
Rubin A. et al., 2016, ApJ, 820, 33
Sahu D. K., Anupama G. C., Srividya S., Muneer S., 2006, MNRAS, 372, 1315
Sanders N. E. et al., 2015, ApJ, 799, 208
Sapir N., Waxman E., 2017, ApJ, 838, 130
Schawinski K. et al., 2008, Science, 321, 223
Schlafly E. F., Finkbeiner D. P., 2011, ApJ, 737, 103
Smartt S. J., 2009, ARA&A, 47, 63
Smartt S. J., 2015, Publ. Astron. Soc. Aust., 32, e016

Sorce J. G., Tully R. B., Courtois H. M., Jarrett T. H., Neill J. D., Shaya E. J., 2014, MNRAS, 444, 527
Takáts K. et al., 2014, MNRAS, 438, 368
Tomasella L. et al., 2013, MNRAS, 434, 1636
Valenti S. et al., 2014, MNRAS, 438, L101
Valenti S. et al., 2015, MNRAS, 448, 2608
Valenti S. et al., 2016, MNRAS, 459, 3939
Van Dyk S. D. et al., 2012, ApJ, 756, 131
Wang X. et al., 2008, ApJ, 675, 626
Zheng X.-M., Zhang J.-J., 2016, Astron. Telegram, 8584

This paper has been typeset from a TEX/LATEX file prepared by the author.